Identification of Atovaquone, Ouabain and Mebendazole as FDA Approved Drugs Targeting SARS-CoV-2 (Version 4)

Ayman B. Farag[1*], Ping Wang[1*], Ian N. Boys[2*], Jennifer L. Eitson[2], Maikke B. Ohlson[2], Wenchun Fan[2], Matthew B. McDougal[2], Mahmoud S. Ahmed[1#], John W. Schoggins[2#], and Hesham A. Sadek[1,3,4,5#]

Departments of Internal Medicine[1], Microbiology[2], Molecular Biology[3], Biophysics[4], and Center for Regenerative Science and Medicine[5], University of Texas Southwestern Medical Center, Dallas, Texas 75390, USA

* Authors contributed equally

Corresponding authors

Correspondence:

Mahmoud S. Ahmed, PhD
Department of Internal Medicine/Division of Cardiology
University of Texas Southwestern Medical Center
6000 Harry Hines Blvd
Dallas, Texas, 75390, USA
Email: Mahmoud.ahmed@utsouthwestern.edu

John W. Schoggins, PhD
Department of Microbiology
University of Texas Southwestern Medical Center
Dallas, Texas, 75390, USA
Email: john.schoggins@utsouthwestern.edu

Hesham A. Sadek, MD, PhD
Departments of Internal Medicine/Division of Cardiology,
Molecular Biology and Biophysics
University of Texas Southwestern Medical Center
6000 Harry Hines Boulevard
Dallas, Texas, 75390, USA
Email: hesham.sadek@utsouthwestern.edu

Abstract

The newly emerged coronavirus, SARS-CoV-2, and the resulting COVID-19 disease, has spread swiftly across the globe since its initial detection in December 2019. Given the heavy toll of this pandemic, therapeutic options for treatment are urgently needed. Here, we adopted a repositioning approach using in-silico molecular modeling to screen FDA-approved drugs with established safety profiles for potential inhibitory effects against SARS-CoV-2. We used structure-based drug design to screen more than 2000 FDA approved drugs against SARS-CoV-2 main protease enzyme (M^{pro}) substrate-binding pocket, focusing on two potential sites (central and terminal sites) to identify hits based on their binding energies, binding modes, interacting amino acids, and therapeutic indications. We additionally screened the top hits from both sites for potential covalent binding via nucleophilic thiol attack of Cys 145. High-scoring candidates were then screened for antiviral activity against infectious SARS-CoV-2 in a cell-based viral replication assay, and counterscreened for toxicity. Atovaquone, Mebendazole, and Ouabain exhibited antiviral efficacy with IC50s well within their respective therapeutic plasma concentrations (low nanomolar to low micromolar range), and limited toxic effects. Notably, all three were predicted in docking studies to covalently bind SARS-CoV-2 M^{pro}, underscoring the utility of this in-silico approach for identifying putative antivirals for repurposing. These results do not confirm efficacy in animal models or in humans, but rather serve as a starting point for testing the antiviral potential of select FDA-approved drugs, either individually or in combination.

Introduction

A newly emerged coronavirus, SARS-CoV-2, was identified in late December 2019 as the etiological agent of a severe acute respiratory disease named COVID-19 [1-3]. The virus has since propagated worldwide, causing an unprecedented incidence of morbidity and mortality in humans. Efforts to discover potential vaccines and therapeutics are still ongoing, with certain therapies such as remdesivir, showing some promise at reducing disease symptoms in COVID-19 patients [4, 5]. However, no treatment or prophylaxis with clear evidence of clinical benefit across large populations of COVID-19 patients has emerged. Additionally, a deeper understanding of the virological properties of SARS-CoV-2 and the full clinical spectrum of COVID-19 disease will take time. Similarly, developing and widely distributing effective vaccines or novel antiviral drugs is unlikely to occur during this season, which leaves healthcare systems vulnerable and the human population at high risk of mortality. As an alternative to de novo drug screening, drug-repurposing strategies can create viable path towards identifying potential therapeutics that have established safety profiles and that can be used individually or in combination for targeting viral proteins or host factors required for viral replication [6-11]. Indeed, to date, several strategies to identify and possibly repurpose drugs for SARS-CoV-2 have been reported [12-21].While these strategies are unlikely to provide immunity or cure, they may identify therapeutics that can alter the clinical course of COVID-19, especially in critically ill patients.

SARS-CoV-2 is a betacoronavirus and its genome encodes several structural proteins, including the glycosylated spike (S) protein that mediates viral attachment to the cells by binding to angiotensin-converting enzyme 2 (ACE2), a membrane bound carboxypeptidase [7, 22, 23]. Viral entry also appears to be mediated by priming of S protein facilitated by the host cell-produced serine protease TMPRSS2 [22, 24]. In addition, the viral genome also encodes nonstructural proteins including an RNA-dependent RNA polymerase (RdRp), main protease (M^{pro}), and papain-like protease (PLpro)[8, 25, 26]. Therefore, targeting ACE2, TMPRSS2, RdRp, M^{pro}, and PLpro, as individual targets, or in combination, may be a viable strategy for repurposed drugs.

Herein, our structure based drug design approach is focused on targeting SARS-CoV-2 M^{pro}

based on the elegant work that resulted in solving the crystal structure of M^{pro} in complex with an inhibitory peptide N3 (PDB ID: 6LU7). Notably, the inhibitory peptide binds the substrate-binding pocket of COVID-19 M^{pro}. This domain was the focus of our screen with regards to the potential hydrophobic binding domain and considering the hydrogen bond network. Starting with the published crystal structure provided us with structural insights for the catalytic binding domain and active druggable sites, elucidating free binding energies with respect to binding affinity and interactions. Additional computational analyses revealed candidate drugs with predicted potential to covalently bind M^{pro}. Select compounds from the docking strategies were tested for antiviral activity against SARS-CoV-2 in a cell based assay. Our studies reveal that several drugs with putative covalent docking modes inhibit SARS-CoV-2 with limited toxic effects on cells. Of these, Atovaquone has a particularly attractive safety profile in humans and known utility in treating a type of pneumonia caused by a fungal infection. Our findings may therefore serve as a starting point to accelerate the use of clinically approved therapeutics in the setting of a pandemic. They may also highlight important pharmacophore features that may aid in the generation of novel molecules that target SARS-CoV-2.

Results

The structural analysis for the peptide ligand N3 co-crystallized along with COVID-19 virus M^{pro} substrate-binding pocket revealed the significance of hydrophobic interactions and hydrogen bond network comprising His163, His164, Glu166, Gln189, and Thr190[11]. We decided to conduct an *in-silico* molecular modeling study for >2000 FDA approved drugs focusing on two potential sites of the M^{pro} substrate-binding pocket based on the co-crystallized peptide N3.

Central site molecular docking:

The central site docking results showed the top 11 hits based on their S score, binding affinity, interacting amino acids, and binding mode to fit the main protease pocket with respect to the reported clinical indication, as shown in **Table 1**. The rest of the top 100 hits are listed in Table S1. Our two and three-dimensional analysis for the top hits is shown in **Figures 2 and 3**. Darunavir, a known antiviral with protease inhibitory mode of action [27], showed the best binding affinity in terms of hydrophobic-hydrophobic and hydrogen bond interactions with

His163, Glu166, and Thr190 at S score -14.03040 Kcal/mol. The top candidates also included antivirals such as Nelfinavir and Saquinavir at S score ranging from -13.4200 Kcal/mo to -12.0917 Kcal/mol. The current repurposing study also includes other drugs approved for different clinical indications. For example, Moexipril, an ACE inhibitor [28], showed a proper binding mode via hydrophobic interactions and a hydrogen bond through a carboxylic acid moiety with Gln189 at S score -13.2142 Kcal/mol. Daunorubicin and Mitoxantrone are representatives for anthracene glycosidic chemotherapeutic agents[29, 30]. Daunorubicin showed potential binding affinity via hydrophobic interactions and hydrogen bonding with Asn142 and Glu166. Mitoxantrone showed hydrophobic interactions and a network of hydrogen bonds with His41, His164, Asp187, Thr190, and Gln192. The anthracene derivatives findings suggest that glycoside-based derivatives can target the substrate-binding pocket of COVID-19 virus M^{pro}. However, administration of chemotherapeutic agents can lead to significant adverse effects and is unlikely to be of any clinical utility in critically ill COVID-19 patients. Metimazole, a pyrazolone based derivative [31], showed a potential binding affinity via hydrogen bonds between a sulphonic acid moiety and His 163 and Ser144 in addition to pi-pi interaction with His41. Although theoretically metamizole might have clinical utility here, it is also not an ideal candidate due to its association with agranulocytosis, which would be an unwelcomed side effect in COVID-19 patients. Bepotastine, an anti-histamine [32, 33], exhibited proper binding affinity in the main substrate-binding pocket via hydrophobic interactions and hydrogen bonding through a carboxylic acid moiety with Gln189. Atovaquone, an antimalarial, drug [34] showed a potential binding affinity with no hydrogen bonds with an S score -8.4159 Kcal/ mol. Rosuvastatin, which belongs to the statins class of antihyperlipidemic drugs [35] displayed an excellent binding affinity in terms of free energy with an S score of -12.3096 Kcal/mol. The Rosuvastatin skeleton filled the entire substrate-binding pocket via hydrophobic interactions and hydrogen bonding with Gly143 and Glu166.

Thus, structure-based drugs design for the top hits targeting the central site of the substrate binding pocket elucidated the following preliminary pharmacophore features: (1) The entire pocket needs hydrophobic features or extended phenyl moieties to maintain a proper binding affinity such as in case of anthracene derivatives. (2) A network of hydrogen bonds (whether donors or acceptors) is a significant factor especially with amino acids Glu166, Gln189, His163, and His164. (3) The presence of terminal sulphonic acid and/or carboxylic acid moie-

ties (Bepotastine, Moexipril, Metimazole, and Rosuvastatin) can act as bio-isosteric moieties to the phosphate groups that can be found in antiviral drugs.

Terminal site molecular docking:

The terminal site of M^{pro} substrate-binding pocket results showed the top 8 hits based on their S score, binding affinity, interacting amino acids, and binding mode to fit the terminal portion with respect to the reported clinical indication, as shown in **Table 2**. Our two and three-dimensional analysis for the top hits targeting the terminal site is shown in **Figures 4 and 5**. Montelukast, an anti-asthmatic drug, showed the best binding affinity in terms of hydrophobic-hydrophobic and hydrogen bond interactions with Thr24, Ser46, and Gln 189 at S score -11.8226 Kcal/mol. A recent report also showed the binding affinity of Montelukast to the same binding domain[36]. Lisinopril, an ACE inhbitor, showed proper binding mode via hydrophobic interactions and a hydrogen bond through a carboxylic acid and amine moieties with Thr26 and His164, respectively at S score -11.5878 Kcal/mol. Bumetanide, a loop diuretic showed a hydrogen bond network with Ser144, His 163, Glu166, and Gln189; in addition to pi-pi interaction along with His41 at S score -11.3008 Kcal/mol. Fexofenadine, an anti-histaminic, protrudes towards the terminal groove of the protease binding pocket with hydrophobic-hydrophobic interactions and hydrogen bond with Thr26 at S score -10.8085 Kcal/mol. Pirbuterol, another anti-asthma with β2 adrenergic activity, bound to the terminal site without further protrusion towards the center with hydrogen bonds Thr24, Thr25, and Ser46. Finally, Bosentan, an endothelin receptor antagonist used for pulmonary arterial hypertension, and quinidine showed hypdrophobic interactions with no hydrogen bonds at S score -10.0878 Kcal/mol and -9.0607 Kcal/mol. Although the dimensional size of the terminal site is limited compared to the central site for the M^{pro} substrate-binding domain, the key amino acid residues for binding are Thr24, Thr25, Thr26, and Ser46.

Covalent molecular docking:

Finally, we performed an independent covalent docking study to identify FDA drugs that can target Cys145 within the substrate-binding pocket, especially given that the co-crystallized inhibitor is peptide in nature (α ketoamide) with covalent mode of binding [37]. We screened the top 200 drugs that resulted from the central and terminal molecular docking (top 100 for each) for targeted covalent docking through Cys 145 via DOCKTITE's protocol by Molecular Operating Environment (MOE) [38]. This resulted in identifying 30 drugs that demonstrated

possible nucleophilic attack by Cys 145 and undergo covalent docking to generate R and S stereo-isomers. Only 9 candidates showed promising binding affinity with respect to S score and covalent binding ability. Our two and three-dimensional analysis for the top 9 covalent hits targeting Cys 145 is shown in **Figures 6 and 7**.

Antiviral activity assay:

After completing in silico docking studies, we next used a cell-based assay to test the antiviral activity of selected compounds against SARS-CoV-2. An isolate of SARS-CoV-2 (USA-WA1/2020) was obtained and propagated in Vero E6 cells [39]. For initial drug screening, Vero E6 were infected with SARS-CoV-2 at 0.1-0.25 multiplicity of infection (MOI). After 1 hr, media containing drugs covering a 6-$\log_{10}$ dilution series was added to the cells. Total RNA from virally infected cells was isolated 24h post-infection and viral RNA replication was quantified by RT-qPCR using Taqman probes. In parallel studies, drugs were screened for effects on cell viability and cellular metabolism by quantifying lactate dehydrogenase (LDH) release and cellular ATP levels (Cell Titer Glo), respectively.

From the 11 drugs identified by the central site docking method, we observed dose-dependent inhibition of SARS-CoV-2 with Atovaquone, Mitoxantrone, Daunorubicin, and Nelfinivir (**Figure 8**). LDH release assays showed that Daunorubicin and Nelfinivir were toxic to cells at high doses, whereas Atovaquone and Mitoxantrone did not elicit substantial LDH release. However, both of these drugs did have effects on cellular ATP levels, consistent with previous reports of the metabolic effects of these compounds [40-44]. Notably, Atovaquone was also predicted to covalently bind the M^{pro} substrate-binding pocket (**Figure 6, 7**). For 7 of the drugs identified by the terminal site docking method, Quinidine and Bosentan exhibited modest dose-dependent antiviral effects with minimal impact on LDH release and cellular ATP levels (**Figure 9**). Quinidine was reported in another drug screening study as a candidate antiviral for SARS-CoV-2 [21]. For the top 7 of drugs that were predicted to exhibit covalent binding, we observed dose-dependent inhibition with Atovaquone, Ouabain, Dronedarone, Mebendazole, and Dronedarone, although Dronedarone appeared to be particularly particularly toxic to cells (**Figure 10**). Interestingly, Ouabain, a cardiac glycoside, has recently been reported to inhibit SARS-CoV-2 infection [14, 45]. Together, 3 of the 7

covalent docking drugs (Atovaquone, Ouabain, and Mebendazole) exhibit antiviral effects in the absence of overt toxicity, suggesting a high hit rate for the in silico analysis.

We next sought to validate several covalent docking candidates and determine IC50s over a 10pt-dose response. Viral infections were performed as described above in Vero E6 and human hepatoma Huh7.5 cells, followed by treating cells with 3-fold dilutions of Atovaquone, Ouabain, Dronedarone, and Mebendazole, starting at 100μM, or in one set of experiments, 200μM Atovaquone. In both cell lines, all drugs tested recapitulated initial findings, though Mebendazole had less antiviral activity in Huh7.5 cells as compared to Vero E6 cells (**Figure 11**). We determined the following IC50s: Atovaquone (1.5 μM in Vero E6, 6.8 μM in Huh7.5); Ouabain (0.030 μM in Vero E6, 0.075 μM in Huh7.5); Dronedarone (1.5 μM in Vero E6, 0.38 μM in Huh7.5 – however the antiviral was likely secondary to cell toxicity); Mebendazole (0.25-1.2 μM in Vero E6, but does not appear to have a strong inhibitory activity on Huh7.5 cells).

We next sought to visually demonstrate the antiviral effect of Atovaquone by indirect immunofluorescence, staining for virus-generated double-stranded RNA (dsRNA) using a dsRNA-specific monoclonal antibody. We tested Atovaquone at 2.5μM and 7.5μM in Vero E6 cells and at 10μM in Huh7.5 cells transduced with lentivirus expressing the SARS-CoV-2 receptor ACE2. All drug-treated cells showed a striking reduction in dsRNA staining as compared to DMSO-treated control cells (**Figure 12**).

Conclusion:

Our studies demonstrate that screening FDA approved drugs against the SARS-CoV-2 virus M^{pro} substrate-binding pocket can identify candidate compounds with validated antiviral effects against infectious SARS-CoV-2 in cultured cells. This approach provides valuable insights to fast-track clinical trials for drugs with an established safety profile. Several top hits from our screen may have potential clinical utility in COVID-19 patients given their known safety profiles for other indications. Indeed, Atovaquone is particularly attractive for several reasons: 1) It is predicted to covalently bind the substrate binding pocket of M^{pro}, raising the prospect that antiviral effects may be durable and difficult for the virus to overcome through

mutation. 2) The IC50 for Atovaquone against SARS-CoV-2 is 1.5 μM, which is well within its therapeutic plasma concentration of approximately 40 μM. Atovaquone also has a high volume of distribution suggesting significant tissue accumulation [46] [47] [48]. 3) Even if Atovaquone does not validate as a true covalent docking drug in pending biochemical studies, it has been previously reported to have antiviral activity against other RNA viruses, by modulating cellular nucleotide pools in a manner that disfavors viral replication [49]. Thus Atovaquone may have two independent antiviral activities, direct effects on M^{pro} and indirect effects on cellular processes required for efficient viral replication. 4) Atovaquone is a well-tolerated, orally available drug that is used to treat PJP. It is thus already indicated for treatment of another infectious disease that affects lung tissue.

Of the remaining 3 top hits, Dronedarone is unlikely to have a real therapeutic value in vivo given that its antiviral activity tracks with its cellular toxicity, and its therapeutic plasma concentration (less that 300 nM[50]) is significantly lower than the measured IC50 of 1.5 μM. Mebendazole is a viable therapeutic option as it is widely available worldwide for treatment of parasitic diseases, and its IC50 of 0.25-1.2 μM in Vero E6 cells falls within its peak plasma concentration of 0.059 to 1.69 μM [51], although it appears less effective in the human cell line Huh7.5 and thus further studies on other types of human cells are needed. Ouabain might also be an attractive therapeutic option given that the IC50 for Ouabain is in the low nanomolar range, well within its therapeutic plasma concentrations [52]. However Ouabain has a narrow therapeutic index, which may limit its use in critically ill patients especially those with impaired renal function or significant electrolyte abnormalities. Ouabain is also not currently approved for use in the US.

Future efficacy studies in animal models and clinical trials in humans are needed to determine whether the drugs identified here could be used alone or in combination as a treatment for COVID-19.

Materials and Methods:

FDA approved small molecules preparation: The U.S. FDA approved drug database was downloaded (drugbank.ca) and 3D structures were energy minimized using MMFF94 force field.

X-ray crystal structure preparation: Crystal structure of COVID-19 virus M^{pro} co-crystallized with an inhibitor has been resolved and accessed via PDB ID: 6LU7. A box was assigned for docking procedures within the hydrophobic binding domain of the peptide inhibitor.

Structure based *in-silico* screening and scoring: The whole energy minimized library was enrolled in docking simulations using Molecular Operating Environment (MOE) along with PDB ID: 6LU7. The energy-minimized drugs underwent protonation states to add the missing hydrogens for proper ionization states. MOE docking module used to evaluate the favorable binding conformers based on London dG scoring method to estimate energy profile based on the binding affinity with respect to hydrophobic-hydrophobic interactions, hydrogen bonding, pi-pi interactions, and ionic interactions [53]. Each drug gave 10 possible docked poses. The ideal pose for each drug was selected according to the similarity of its binding mode in the binding pocket to that of the co-crystallized peptide. Two dimensional diagrams were generated using MOE tools, while three dimensional figures were generated using pymol.

Covalent Docking using DOCKTITE: The covalent docking protocol will filter the top 200 FDA drug candidates combining automated warhead screening to reveal 31 candidates that can undero nucleophilic attack by Cys 145 based on their chemical structure, nucleophilic side chain attachment with the right configuration (R or S), pharmacophore-based docking, and the chimeric poses will undergo consensus scoring approach using MOE-internal empirical scoring functions and the external knowledge-based scoring function drug score extended (DSX) that consists of distance-dependent pair potentials, novel torsion angle potentials, and newly defined solvent accessible surface-dependent potentials [54]. The validation step will include pose predictions of 10 protein/ligand complexes with a cutoff mean RMSD of 2 A°.

Virus and cells: SARS-CoV-2 (strain USA-WA1/2020) was obtained from the World Reference Center for Emerging Viruses and Arboviruses, University of Texas Medical Branch. Virus was propagated by low MOI infection (MOI 0.01-0.001) in VeroE6 cells. When 70-90% CPE was observed (48-72h post-infection), virus-containing supernatant was harvested, aliquot, and stored at -80C until use. Viral titers were determined by TCID50 assay. VeroE6 cells (from C. Rice, The Rockefeller University) were grown in MEM (Gibco) supplemented with 10% FBS (Gibco) and 1× non-essential amino acids (NEAA; Gibco). Huh7.5 and 293T cells (from C. Rice, The Rockefeller University) were grown in DMEM (Gibco) supplemented with 10% FBS (Gibco) and 1× non-essential amino acids (NEAA; Gibco). Huh7.5 cells stably expressing ACE2 were maintained in DMEM supplemented with 4µg/mL puromycin.

Lentiviral pseudoparticles: Lentiviral pseudoparticles were generated by transfection in 293T cells. Lentiviral pseudoparticles in the pSCRPSY backbone were generated as previously described (PMID 22908290). A plasmid containing ACE2 was a kind gift of Neal Alto (UT Southwestern Medical Center).

SARS-CoV-2 infections: For screens, VeroE6 cells were seeded at 35,000 cells per well on 48 well plates approximately 16-20 hours before infection. Prior to infection, drugs were serially-diluted in media to a concentration of 1.5X target concentration. For screens, 6-point 10-fold dilutions of drug were used, and for validation 10-point 3-fold dilutions were used. VeroE6 cells were incubated with 0.1-0.25 MOI SARS-CoV-2 in a minimum volume of low-serum media for one hour to allow virus to bind and enter cells. Huh7.5 cells were incubated in After viral entry, media containing candidate compounds or vehicle control was added to cells to a final 1X concentration.

RNA isolations: Virus-infected cells were lysed in 300 µl of TRI reagent 24 hours post-infection. Viral RNA was isolated using Direct-zol RNA Miniprep kits (ZymoResearch, #R2053) according to manufacturer's protocol. Total RNA was eluted in 50 µl of DNase/RNase free water.

SARS-CoV-2 positive control: SARS-Cov-2 N gene was amplified from a synthesized N gene fragment (IDT) with primers that introduced a T7 promoter sequence on the 3' end (IDT) (Table S2). PCR product was purified using Qiagen PCR Purification Kit (Qiagen). In vitro

transcription was performed using T7 RiboMAX Express Large Scale RNA Production System following manufacturers protocol (Promega). RNA was quantitated by nanodrop on DS-11 FX and by a fluorometer assay using the DeNovix RNA Assay (DeNovix). In-vitro transcribed RNA was used to generate a standard curve for qPCR from a 10-fold dilution series starting at 5e10 copies of RNA.

RT-qPCR: A 25 µL reaction contained 5 µL RNA, 12.5 µL of 2x reaction buffer (containing 0.4 mM of each dNTP and 6 mM $MgSO_4$), 0.5 µl of a 2.5 µM ROX Reference Dye solution, 0.5 µL SuperScript III RT/Platinum *Taq* Mix (Invitrogen) and 1.8 µL Primer/Probe mix (500µM each primer, 125µM probe). SARS-CoV-2 primers and probe were designed as recommended by the Center for Disease Control (https://www.cdc.gov/coronavirus/2019-ncov/lab/rt-pcr-panel-primer-probes.html). GAPDH primers and probe were designed as published [55] (Table S2). All oligonucleotides were synthesized by LGC Biosearch Technologies. RT was performed at 50°C for 5 minutes, followed by inactivation at 95°C for 2 minutes, and 40 cycles of PCR (95°C for 3 seconds, 60°C for 30 seconds) on an ABI 7500 Fast thermocycler (Applied Biosystems).

Cell viability and cell toxicity assays: VeroE6 cells seeded at 12,000 cells per well in 96-well plates were incubated in the presence of each compound or DMSO as control diluted in MEM/10% FBS for 24 h. To quantify cell lysis, 50 microliters of cell supernatant was assayed for lactate dehydrogenase (LDH) release using the CytoTox 96 (Promega) assay according to manufacturer's instructions. To measure viable cells, the remaining media was aspirated from each well and replaced with 50 microliters of CellTiter-Glo (Promega) reagent diluted 1:1 with MEM/10% FBS, and incubated 10 min. Luminescence was measured for 30 microliters of each sample in a white-walled 96-well plate using a Berthold XS3 LB 960 luminometer.

Immunofluorescence: Cells were fixed with 3.7% formaldehyde in water. Cells were washed with PBS, then permeabilized with 0.2% Triton-X 100. Cells were blocked with 5% goat serum/PBS for at least 30 minutes. Primary antibody (J2, SciCons) was added in blocking solution and incubated for 1 hour. Cells were washed 3x with PBS, after which secondary antibody (Goat-anti-mouse AlexaFluor 488, Invitrogen),was added in 5% BSA/PBS and incubated for 30 minutes. Cells were washed 3x with PBS, and then mounted using Vec-

tasheild Antifade Mounting Reagent with DAPI (VectorLabs). Imaging was performed on a Zeiss Observer Z.1. Images were processed in ImageJ.

Figures:

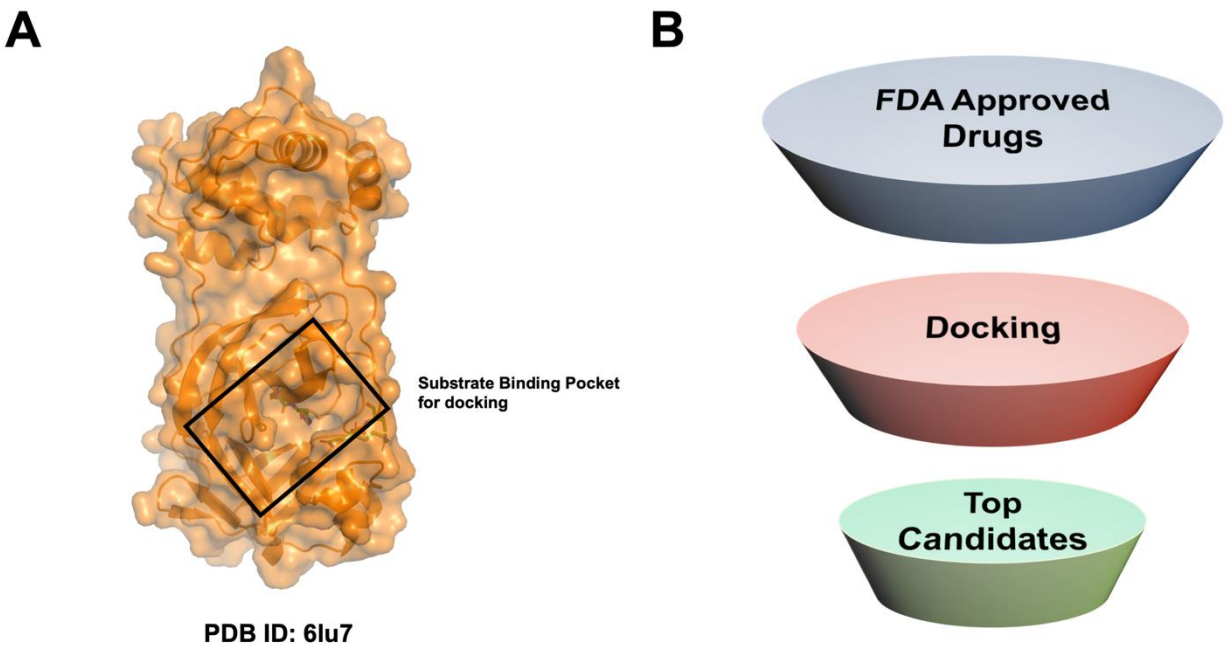

Figure 1. Worklow: **A)** Crystal structure of COVID-19 virus M^{pro} highlighting the substrate binding-pocket which was used for docking. **B)** Schematic diagram for in-silico drug repositioning.

Drug	S score (Kcal / mol)	Clinical Indication
Darunavir	-14.0304	Antiviral
Mitoxantrone	-13.8100	Anticancer
Nelfinavir	-13.4200	Antiviral
Moexpril	-13.2442	Anti-hypertensive
Daunorubicin	-12.5009	Anticancer
Rosuvastatin	-12.3096	Anti-hypercholesterolemia
Saquinavir	-12.0917	Antiviral
Metamizole	-11.6652	Anti-inflammatory
Bepotastine	-10.6350	Anti-histaminic
Benzonatate	-10.4759	Anti-tussive
Atovaqoune	-8.1459	Antimalarial

Table 1. List of top drugs docked to COVID-19 virus M^{pro} substrate-binding pocket (1-12) based on S score.

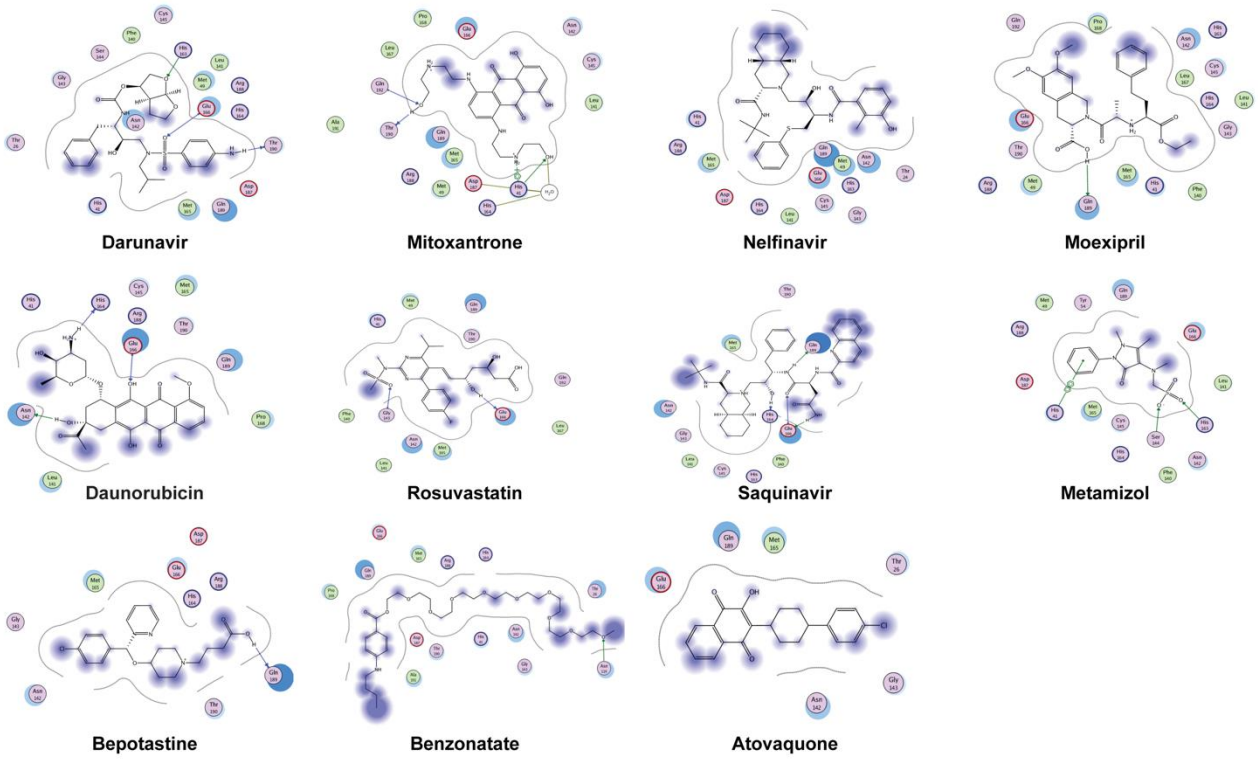

Figure 2. Two-dimensional presentation of docking poses for top 11 candidates targeting central site of protease domain. Blue arrows are backbone hydrogen bonds and green arrows are the side chain hydrogen bonds.

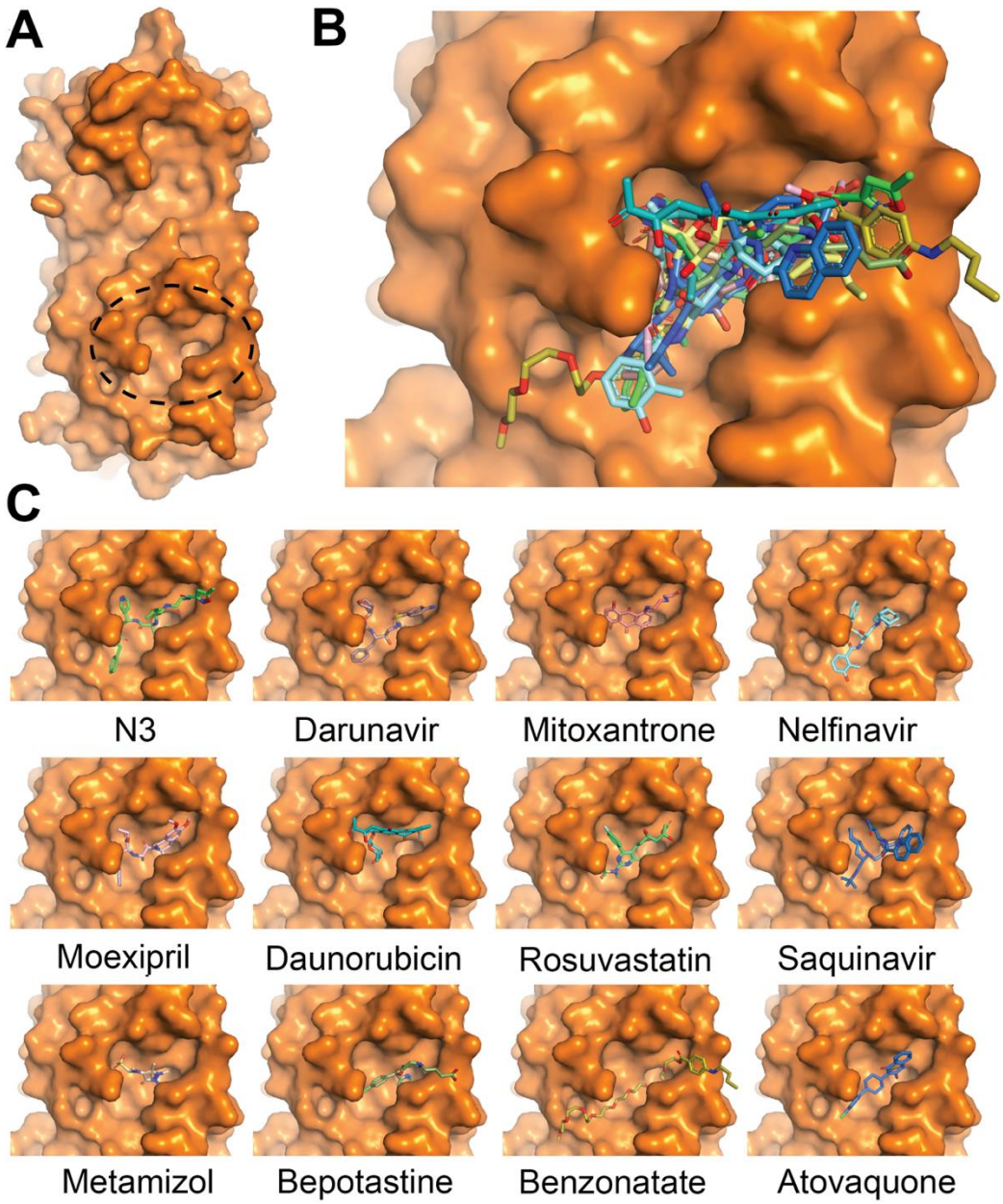

Figure 3. Docked positions to the central site of the substrate binding-pocket of COVID-19 virus M^{pro}: **A)** 3D presentation of the pocket. **B)** Overlayed docked positions of all 11 top hits in addition the previously co-cryslatlized inhibitory peptide N3. **C)** Individual docking positions.

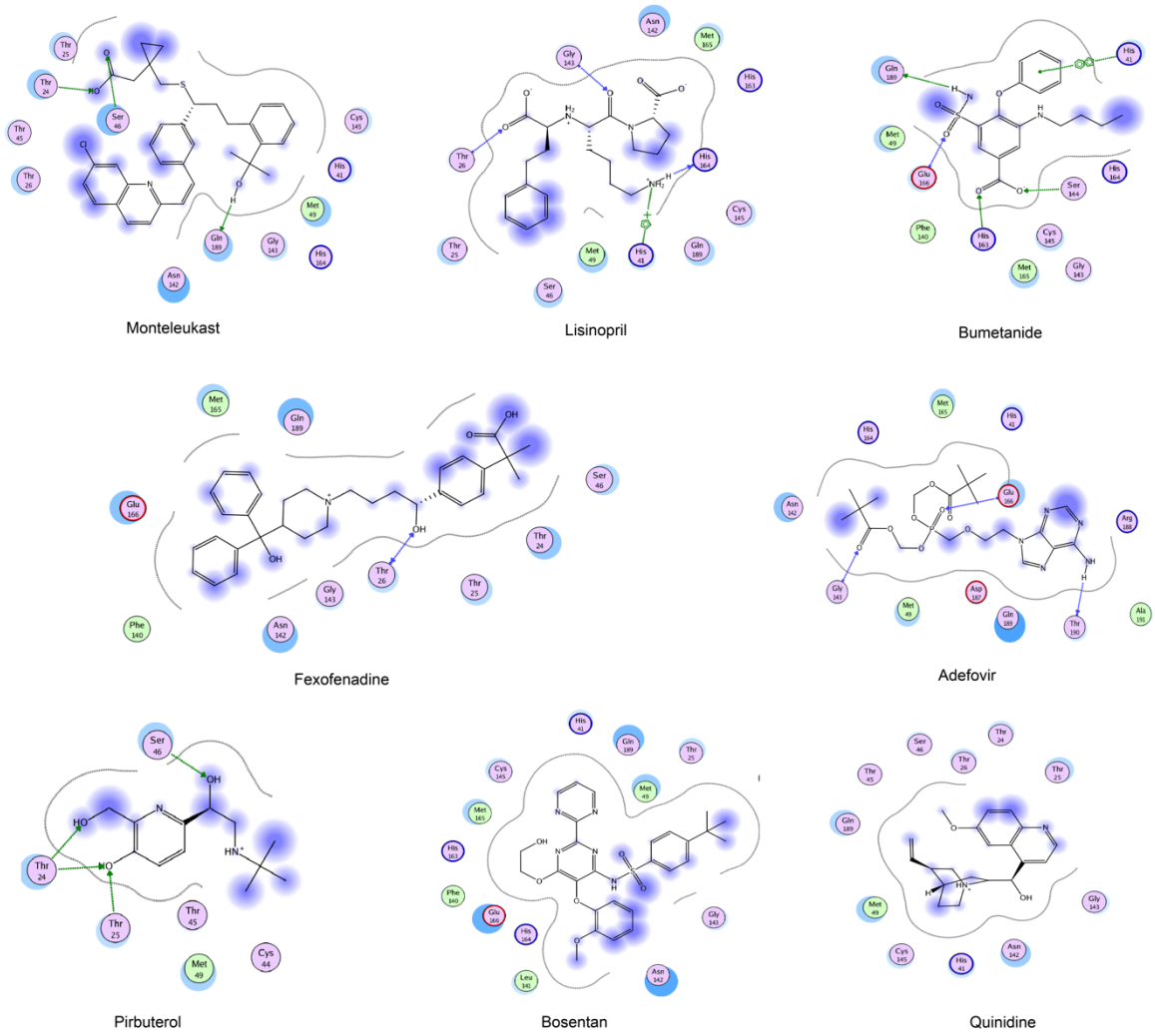

Figure 4. Two-dimensional presentation of docking poses for top 8 candidates targeting terminal site of protease domain. Blue arrows are backbone hydrogen bonds and green arrows are the side chain hydrogen bonds.

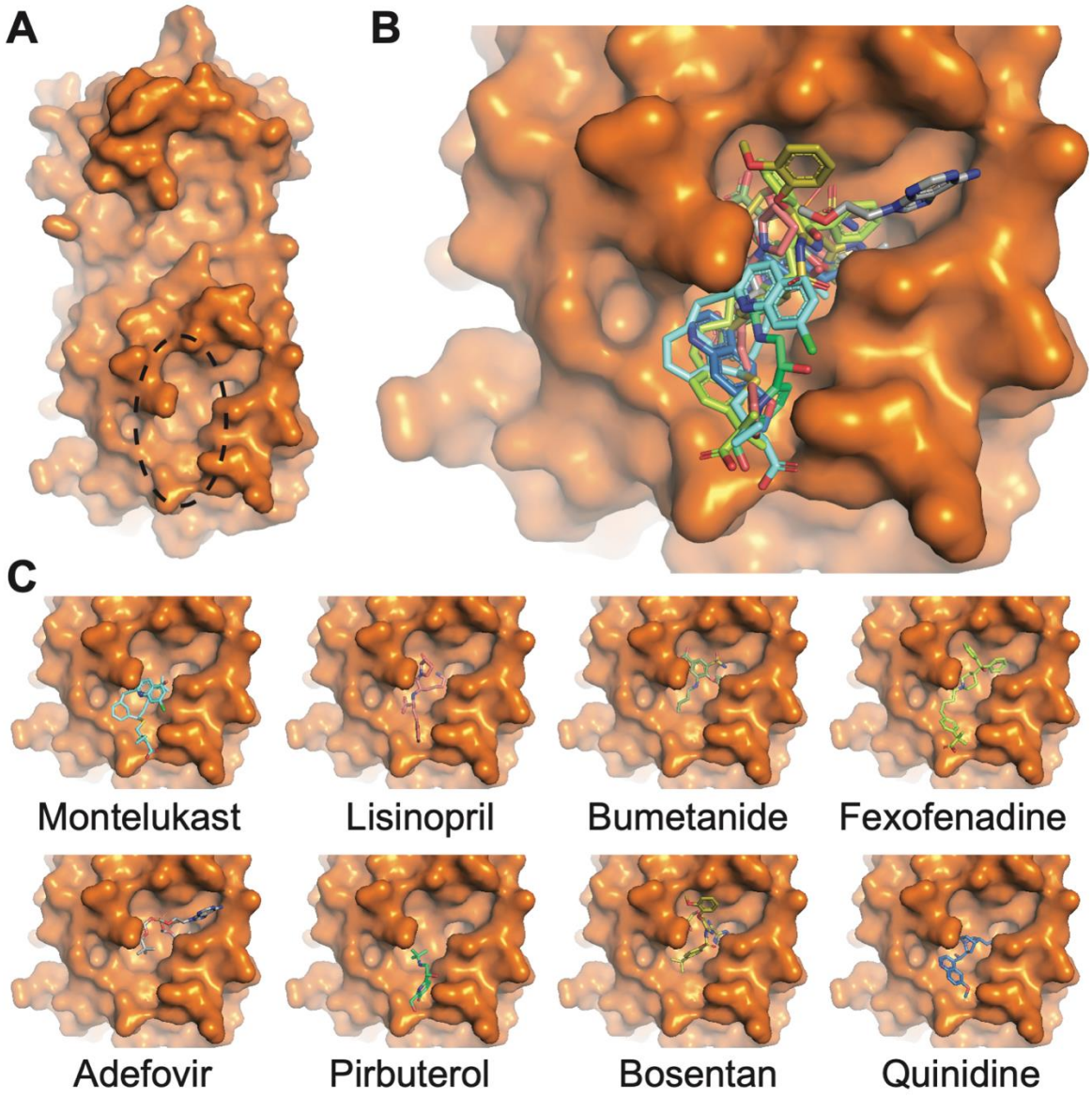

Figure 5. Docked positions to the terminal site for substrate binding-pocket of COVID-19 virus M^{pro}: **A)** 3D presentation of the pocket. **B)** Overlayed docked positions of all 8 top hits in addition to the previously co-crystallized inhibitory peptide N3. **C)** Individual docking positions.

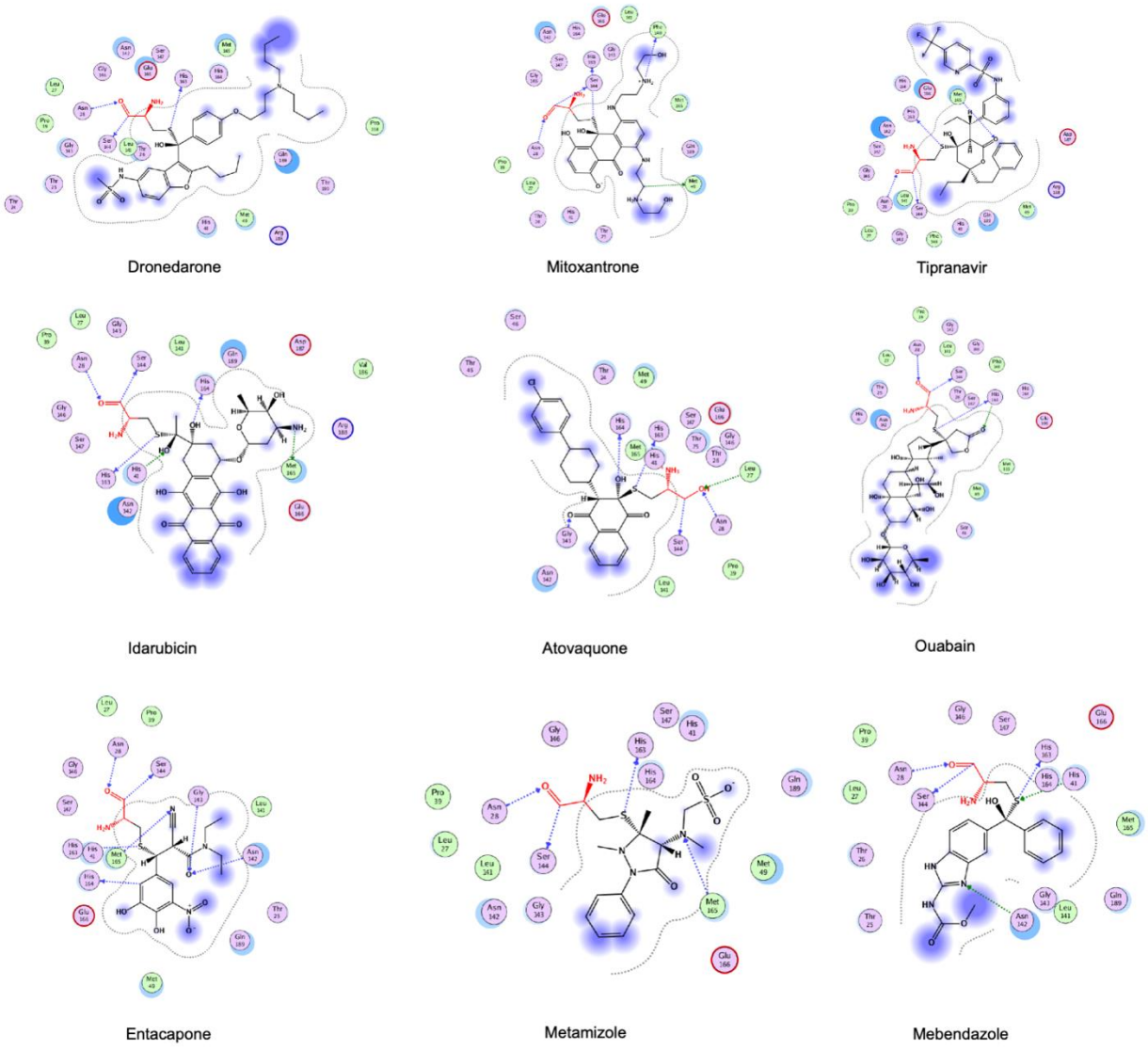

Figure 6. Two-dimensional presentation of covalent docking poses for top 9 candidates targeting Cys 145 of protease domain. Blue arrows are backbone hydrogen bonds and green arrows are the side chain hydrogen bonds.

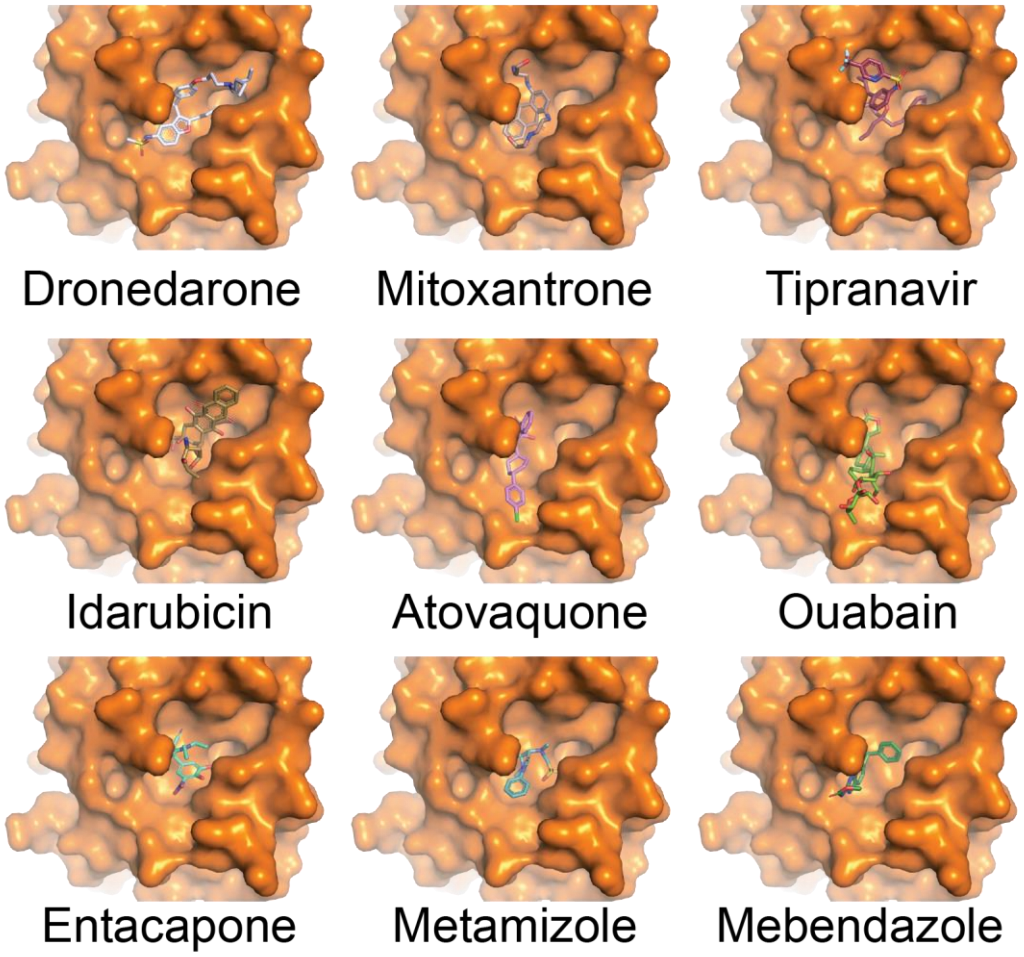

Figure 7. Docked positions for the covalently bound candidates targeting Cys 145 of COVID-19 virus $M^{pro.}$

Drug	S score (Kcal / mol)	Clinical Indication
Montelukast	-11.8226	Anti-asthma
Lisinopril	-11.5878	Anti-hypertensive
Bumetanide	-11.3008	Anti-hypertensive
Fexofenadine	-10.8085	Anti-histaminic
Adefovir	-10.4470	Antiviral
Pirbuterol	-10.3436	Anti-asthma
Bosnetan	-10.0878	Anti-hypertensive
Qunidine	-9.0607	Anti-malarial

Table 2. List of top drugs docked to COVID-19 virus M^{pro} substrate-binding pocket on S score.

Drug	Stereogenic center orientation	S score (Kcal / mol)	Clinical Indication
Dronedarone	R	-12.8752	Antiarrythmic
Mitoxantrone	R	-11.6140	Anticancer
Tipranavir	S	-11.3686	Antiviral
Idarubicin	R	-10.1043	Anticancer
Atovaquone	R	-8.8177	Antimalarial
Ouabin	S	-8.4562	Anticancer
Entacapone	R	-8.2882	COMT inhibitor
Metamizole	R	-82165	Anti-Inflammatory
Mebendazole	R	-7.5352	Anti-parasite

Table 3. List of top drugs docked covalently to Cys 145 of COVID-19 virus M^{pro} substrate-binding pocket showing the configuration of nucleophilic attack and S score.

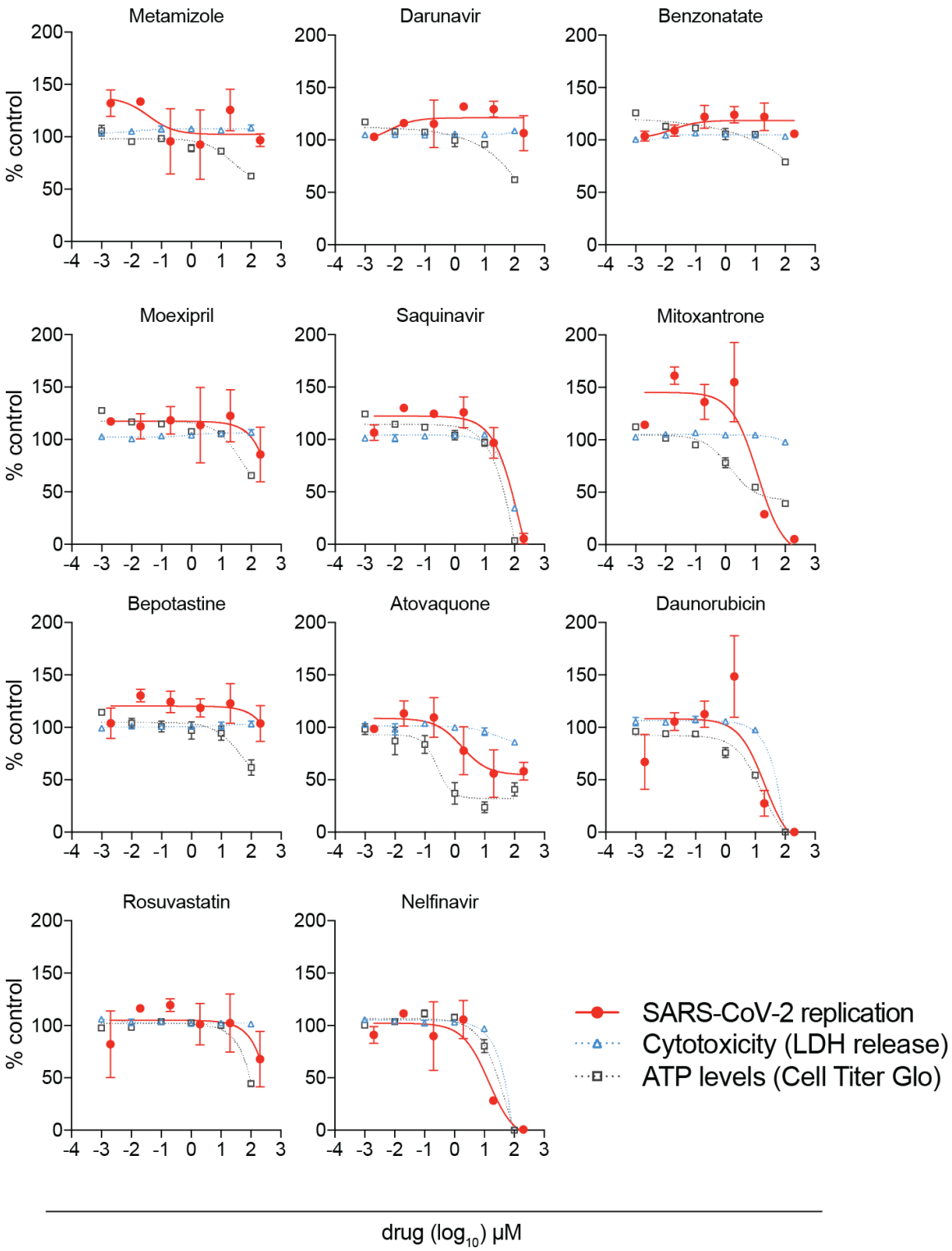

Figure 8. Antiviral activity of drugs identified from central site docking. SARS-CoV-2 replication was quantified by Taqman RT-PCR. Drug-induced effects on cells was monitored by quantifying LDH release and ATP levels. Data represent the averages of two biological replicates.

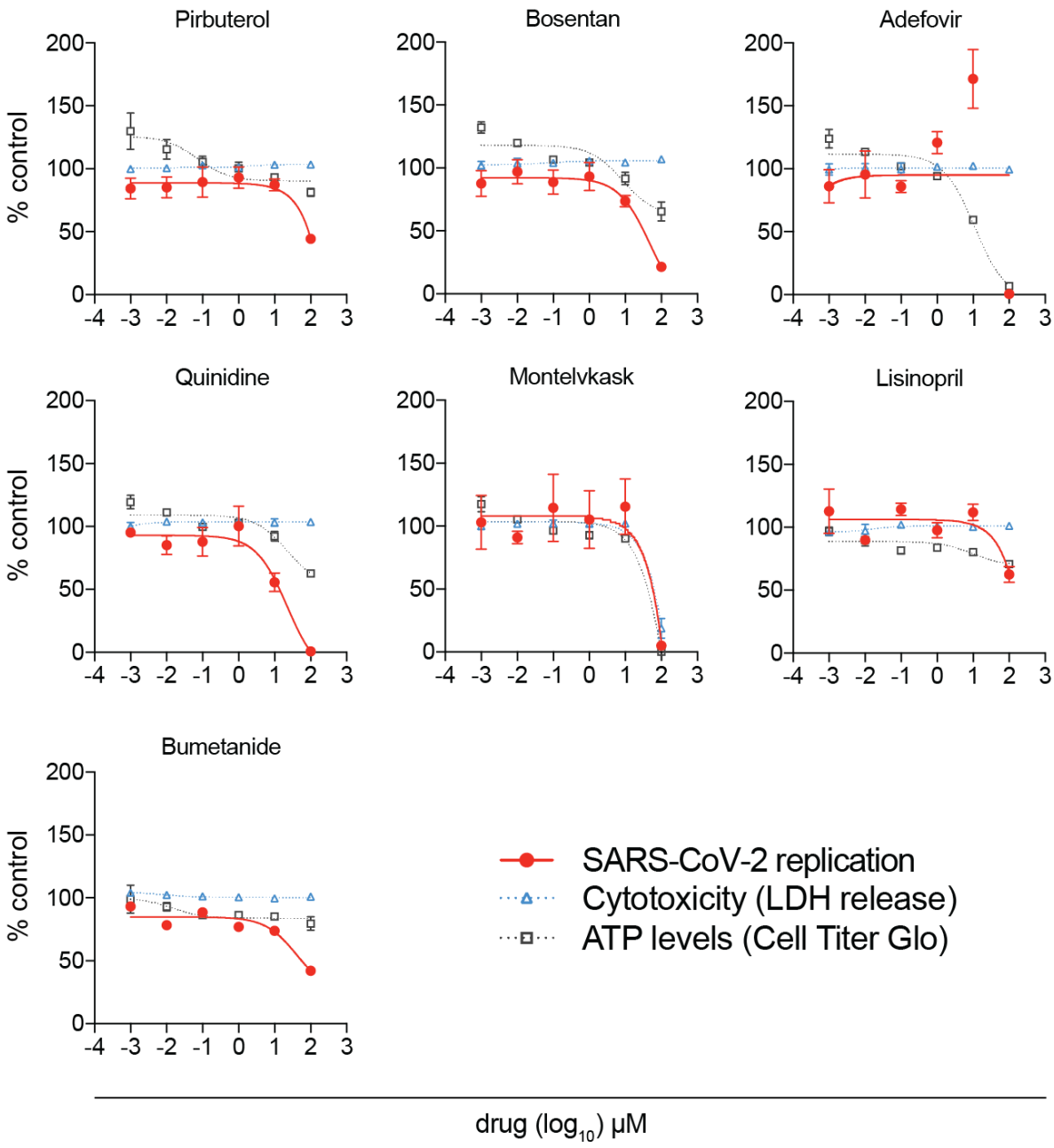

Figure 9. Antiviral activity of drugs identified from terminal site docking. SARS-CoV-2 replication was quantified by Taqman RT-PCR. Drug-induced effects on cells was monitored by quantifying LDH release and ATP levels. Data represent the averages of two biological replicates.

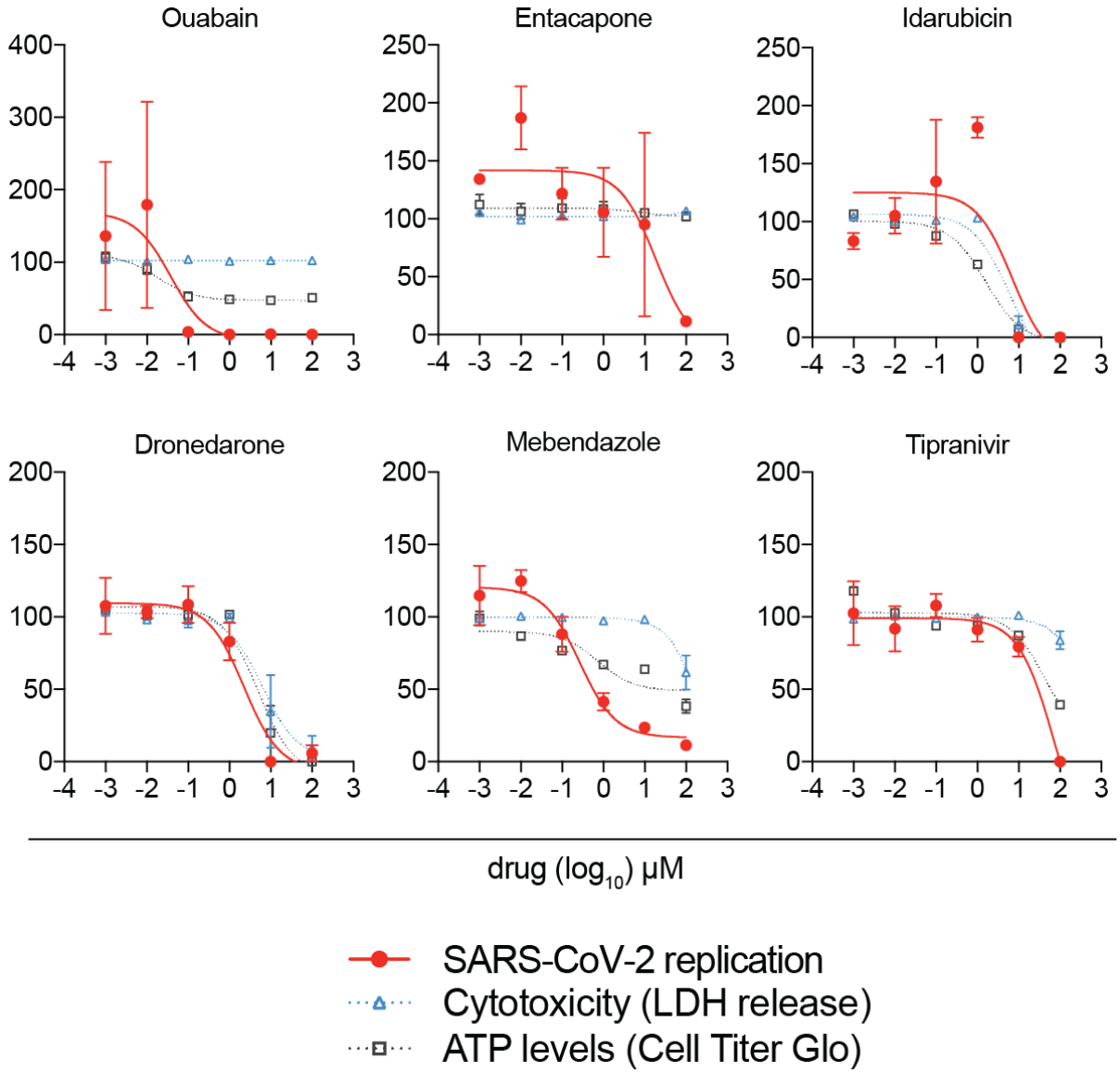

Figure 10. Antiviral activity of drugs predicted to covalently bind to M^{pro} active site. SARS-CoV-2 replication was quantified by Taqman RT-PCR. Drug-induced effects on cells was monitored by quantifying LDH release and ATP levels. Data represent the averages of two biological replicates.

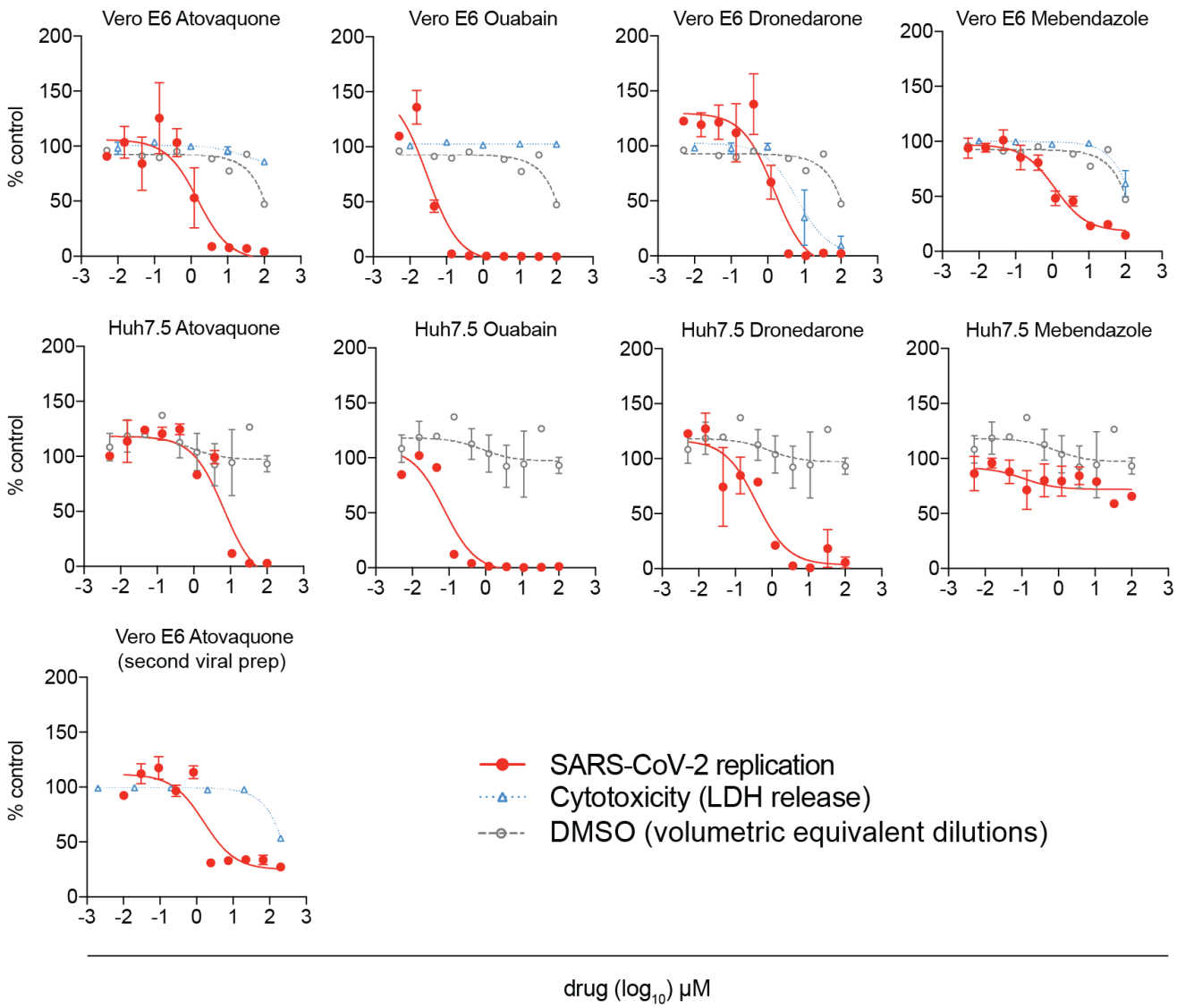

Figure 11. Validation of drugs predicted to covalently bond to M^{pro} active site by 10pt curve analysis in two cell lines. SARS-CoV-2 replication was quantified by Taqman RT-PCR. LDH data are duplicated from previous figures. DMSO is shown as a control for effects of vehicle on infection in Huh7.5 cells. Data represent the averages of three biological replicates for Atovaquone "second viral prep" and two replicates for all others.

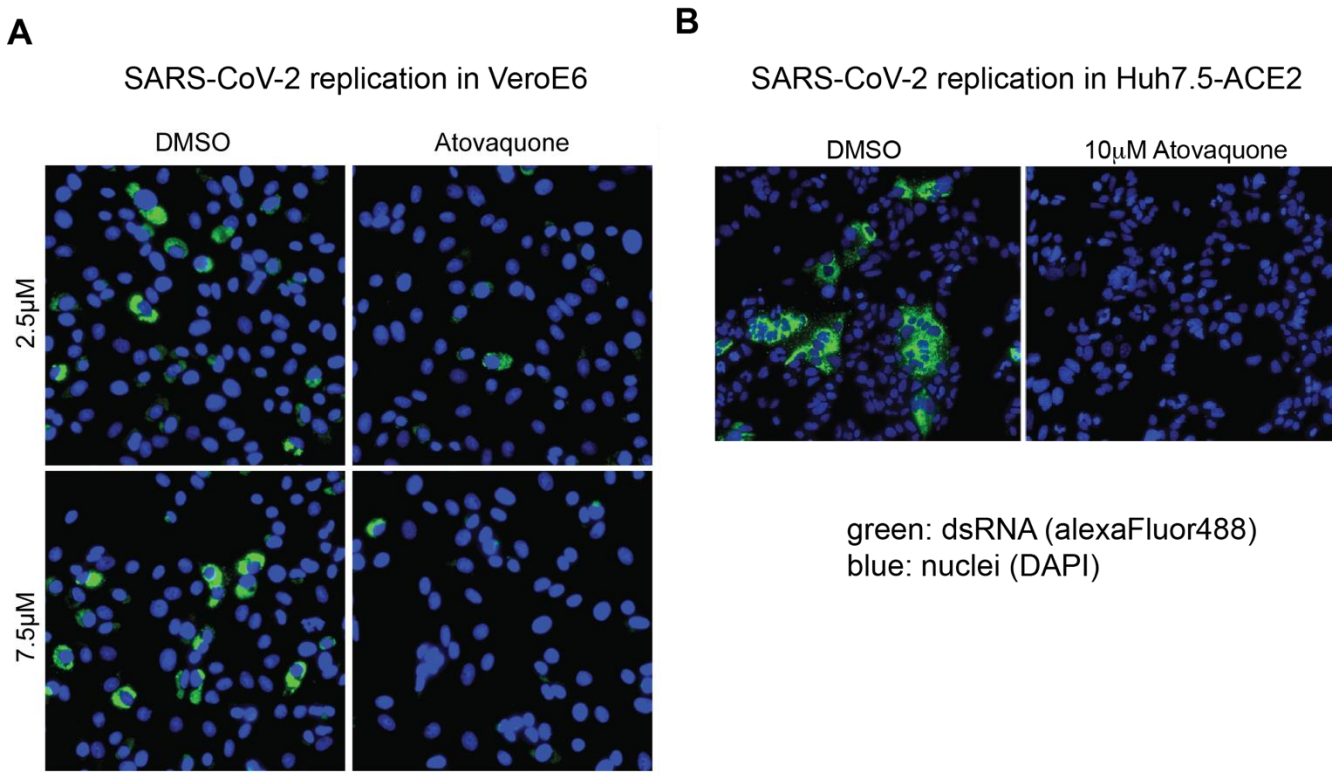

Figure 12. Inhibition of SARS-CoV-2 by Atovaquone in two cell lines. Vero E6 cells were treated with two doses of Atovaquone after infecton with SARS-CoV-2. Cells were processed for staining by immunofluorescence with anti-dsRNA antibody 24 h post-infection. N=1. Huh7.5 cells ectopically expressing ACE2 were treated with one dose of Atovaquone 1h after infection with SARS-CoV-2. Cells were processed for staining by immunofluorescence with anti-dsRNA antibody 10 h post-infection. Data are representative of images obtained from 1 (Vero E6) or 2 (Huh7.5) independent experiments.

Supporting Information:

Table S1. List of the remaining top 100 drugs bound to the centeral site of protease domain based on S score.

Drug	S score (Kcal / mol)
Dipiverfin	-8.1378
Defroxamine	-8.1225
Dobutamine	-8.1108
Metipanolol	-8.0286
Ziprosidone	-8.0030
Cladribine	-7.9624
Almitrine	-7.9462
Epoprostenol	-7.8723
Famciclovir	-7.8672
Fluvastatine	-7.8443
Ticonazole	-7.8416
Delviradine	-7.8185
Methantheline	-7.7925
Mefloquine	-7.7520

Drug	S score (Kcal / mol)
Diatrizoate	-7.6401
Iloperidone	-7.6082
Sapropterin	-7.5764
Vincristine	-7.5485
Oxamniquine	-7.54058
Teniposide	-7.5293
Abacavir	-7.4897
Zoledronic acid	-7.4834
Etoposide	-7.4235
Carbetocin	-7.4149
Adefovir	-7.3944
Desoximetasone	-7.3692
Timolol	-7.3641
Loratadine	-7.2958
variconazole	-7.2894
Tipranvir	-7.2732
Chloroquine	-7.2639

Drug	S score (Kcal / mol)
Indometacin	-7.2021
Meloxicam	-7.2002
Labetolol	-7.2001
Deslanoside	-7.1533
Leflunomide	-7.1231
Pimozide	-7.0937
Repaglinide	-7.0160
Furosemide	-6.9690
Candoxatril	-6.8322
Indapamide	-6.8165
Lansoprazole	-6.8003
Simvastatin	-6.7121
Cilizapril	-6.6663
Fosinopril	-6.4010
Donedarone	-6.2281
Indinavir	-6.2012
Paricalcitol	-6.1779

Drug	S score (Kcal / mol)
Imodium	-6.1374
Bexarotene	-6.0809
Clofarabine	-6.0798
Betamethasone	-5.9249
Bricodar	-5.7965
Nafareline	-5.7426
Mebendazol	-5.7426
Levocabastine	-5.6281
Losartan	-5.3706
Omapatrilate	-5.3388
Cidofovir	-5.1052
Flecainide	-4.9986

Table S2. Oligos used to generate N gene RNA by T7 transcription

Oligonucleotide	Sequence
T7-SARS-CoV-2_N	TAA TAC GAC TCA CTA TAG GGA TGT CTG ATA ATG GAC CCC AAA ATC AGC
SARS-CoV-2-NotI	CTA ATT GCG GCC GCT TAG GCC TGA GTT GAG TCA GCA C

Table S3. Oligos used for RT-qPCR

Assay	Oligonucleotide	Sequence[a]
SARS-CoV-2	SARS-CoV-2_N1-F	GAC CCC AAA ATC AGC GAA AT
	SARS-CoV-2_N1-R	TCT GGT TAC TGC CAG TTG AAT CTG
	SARS-CoV-2_N1-P	FAM-ACC CCG CAT TAC GTT TGG TGG ACC-BHQ1
GAPDH	GAPDH_F	GAAGGTGAAGGTCGGAGTCAAC
	GAPDH_R	CAGAGTTAAAAGCAGCCCTGGT
	GAPDH_P	JOE-TTTGGTCGTATTGGGCGCCT-BHQ1

[a] FAM: 6-carboxyfluorescein; JOE: 4′,5′-dichloro-2′,7′-dimethoxy-6-carboxyfluorescein, BHQ-1: Black Hole Quencher 1

References:

1. Malik, Y.S., et al., *Emerging novel coronavirus (2019-nCoV)-current scenario, evolutionary perspective based on genome analysis and recent developments.* Vet Q, 2020. **40**(1): p. 68-76.
2. Wu, F., et al., *A new coronavirus associated with human respiratory disease in China.* Nature, 2020. **579**(7798): p. 265-269.
3. Zhou, P., et al., *A pneumonia outbreak associated with a new coronavirus of probable bat origin.* Nature, 2020. **579**(7798): p. 270-273.
4. Grein, J., et al., *Compassionate Use of Remdesivir for Patients with Severe Covid-19.* N Engl J Med, 2020.
5. Wang, Y., et al., *Remdesivir in adults with severe COVID-19: a randomised, double-blind, placebo-controlled, multicentre trial.* The Lancet, 2020.
6. Du, L., et al., *The spike protein of SARS-CoV--a target for vaccine and therapeutic development.* Nat Rev Microbiol, 2009. **7**(3): p. 226-36.
7. Wrapp, D., et al., *Cryo-EM structure of the 2019-nCoV spike in the prefusion conformation.* Science, 2020. **367**(6483): p. 1260-1263.
8. Hoffmann, M., et al., *SARS-CoV-2 Cell Entry Depends on ACE2 and TMPRSS2 and Is Blocked by a Clinically Proven Protease Inhibitor.* Cell, 2020.
9. Anthony, S.J., et al., *Global patterns in coronavirus diversity.* Virus Evol, 2017. **3**(1): p. vex012.
10. Anand, K., et al., *Coronavirus main proteinase (3CLpro) structure: basis for design of anti-SARS drugs.* Science, 2003. **300**(5626): p. 1763-7.
11. Wang, F., et al., *Structure of Main Protease from Human Coronavirus NL63: Insights for Wide Spectrum Anti-Coronavirus Drug Design.* Sci Rep, 2016. **6**: p. 22677.
12. Gordon, D.E., et al., *A SARS-CoV-2 protein interaction map reveals targets for drug repurposing.* Nature, 2020.
13. Lobo-Galo, N., et al., *FDA-approved thiol-reacting drugs that potentially bind into the SARS-CoV-2 main protease, essential for viral replication.* J Biomol Struct Dyn, 2020: p. 1-12.
14. Jeon, S., et al., *Identification of antiviral drug candidates against SARS-CoV-2 from FDA-approved drugs.* Antimicrob Agents Chemother, 2020.
15. Mantlo, E., et al., *Antiviral activities of type I interferons to SARS-CoV-2 infection.* Antiviral Res, 2020. **179**: p. 104811.
16. Riva, L., et al., *A Large-scale Drug Repositioning Survey for SARS-CoV-2 Antivirals.* bioRxiv, 2020: p. 2020.04.16.044016.
17. Matsuyama, S., et al., *The inhaled corticosteroid ciclesonide blocks coronavirus RNA replication by targeting viral NSP15.* bioRxiv, 2020: p. 2020.03.11.987016.
18. Weston, S., et al., *Broad anti-coronaviral activity of FDA approved drugs against SARS-CoV-2 in vitro and SARS-CoV in vivo.* bioRxiv, 2020: p. 2020.03.25.008482.
19. Liu, S., et al., *Evaluation of 19 antiviral drugs against SARS-CoV-2 Infection.* bioRxiv, 2020: p. 2020.04.29.067983.
20. Bukreyeva, N., et al., *The IMPDH inhibitor merimepodib suppresses SARS-CoV-2 replication in vitro.* bioRxiv, 2020: p. 2020.04.07.028589.
21. Touret, F., et al., *In vitro screening of a FDA approved chemical library reveals potential inhibitors of SARS-CoV-2 replication.* bioRxiv, 2020: p. 2020.04.03.023846.

22. Hoffmann, M., et al., *SARS-CoV-2 Cell Entry Depends on ACE2 and TMPRSS2 and Is Blocked by a Clinically Proven Protease Inhibitor.* Cell, 2020. **181**(2): p. 271-280 e8.
23. Yan, R., et al., *Structural basis for the recognition of SARS-CoV-2 by full-length human ACE2.* Science, 2020. **367**(6485): p. 1444-1448.
24. Hoffmann, M., H. Kleine-Weber, and S. Pohlmann, *A Multibasic Cleavage Site in the Spike Protein of SARS-CoV-2 Is Essential for Infection of Human Lung Cells.* Mol Cell, 2020.
25. Gorbalenya, A.E., et al., *Nidovirales: evolving the largest RNA virus genome.* Virus Res, 2006. **117**(1): p. 17-37.
26. Baez-Santos, Y.M., S.E. St John, and A.D. Mesecar, *The SARS-coronavirus papain-like protease: structure, function and inhibition by designed antiviral compounds.* Antiviral Res, 2015. **115**: p. 21-38.
27. Li, D., et al., *Investigation on the mechanism for the binding and drug resistance of wild type and mutations of G86 residue in HIV-1 protease complexed with Darunavir by molecular dynamic simulation and free energy calculation.* J Mol Model, 2014. **20**(2): p. 2122.
28. Kalasz, H., et al., *Metabolism of moexipril to moexiprilat: determination of in vitro metabolism using HPLC-ES-MS.* Med Chem, 2007. **3**(1): p. 101-6.
29. Pang, B., et al., *Drug-induced histone eviction from open chromatin contributes to the chemotherapeutic effects of doxorubicin.* Nat Commun, 2013. **4**: p. 1908.
30. Wu, C.C., et al., *On the structural basis and design guidelines for type II topoisomerase-targeting anticancer drugs.* Nucleic Acids Res, 2013. **41**(22): p. 10630-40.
31. Garcia-Martin, E., et al., *Genetic determinants of metamizole metabolism modify the risk of developing anaphylaxis.* Pharmacogenet Genomics, 2015. **25**(9): p. 462-4.
32. Takahashi, D., et al., *Backbone and side-chain (1)H, (1)(5)N, and (1)(3)C resonance assignments of Norwalk virus protease.* Biomol NMR Assign, 2012. **6**(1): p. 19-21.
33. Takahashi, H., A. Ishida-Yamamoto, and H. Iizuka, *Effects of bepotastine, cetirizine, fexofenadine, and olopatadine on histamine-induced wheal-and flare-response, sedation, and psychomotor performance.* Clin Exp Dermatol, 2004. **29**(5): p. 526-32.
34. Hughes, W., et al., *Comparison of atovaquone (566C80) with trimethoprim-sulfamethoxazole to treat Pneumocystis carinii pneumonia in patients with AIDS.* N Engl J Med, 1993. **328**(21): p. 1521-7.
35. Jones, P.H., et al., *Comparison of the efficacy and safety of rosuvastatin versus atorvastatin, simvastatin, and pravastatin across doses (STELLAR* Trial).* Am J Cardiol, 2003. **92**(2): p. 152-60.
36. Wu, C., et al., *Analysis of therapeutic targets for SARS-CoV-2 and discovery of potential drugs by computational methods.* Acta Pharmaceutica Sinica B, 2020.
37. Zhang, L., et al., *Crystal structure of SARS-CoV-2 main protease provides a basis for design of improved α-ketoamide inhibitors.* Science, 2020: p. eabb3405.
38. Scholz, C., et al., *DOCKTITE-a highly versatile step-by-step workflow for covalent docking and virtual screening in the molecular operating environment.* J Chem Inf Model, 2015. **55**(2): p. 398-406.
39. Harcourt, J., et al., *Severe Acute Respiratory Syndrome Coronavirus 2 from Patient with 2019 Novel Coronavirus Disease, United States.* Emerg Infect Dis, 2020. **26**(6).
40. Fiorillo, M., et al., *Repurposing atovaquone: targeting mitochondrial complex III and OXPHOS to eradicate cancer stem cells.* Oncotarget, 2016. **7**(23): p. 34084-99.
41. Neri, B., G. Cini-Neri, and M. D'Alterio, *Effect of anthracyclines and mitoxantrone on oxygen uptake and ATP intracellular concentration in rat heart slices.* Biochem Biophys Res Commun, 1984. **125**(3): p. 954-60.

42. Shipp, N.G., et al., *Characterization of experimental mitoxantrone cardiotoxicity and its partial inhibition by ICRF-187 in cultured neonatal rat heart cells.* Cancer Res, 1993. **53**(3): p. 550-6.
43. Martins, I., et al., *Chemotherapy induces ATP release from tumor cells.* Cell Cycle, 2009. **8**(22): p. 3723-8.
44. Ashton, T.M., et al., *The anti-malarial atovaquone increases radiosensitivity by alleviating tumour hypoxia.* Nat Commun, 2016. **7**: p. 12308.
45. Ko, M., et al., *Comparative analysis of antiviral efficacy of FDA-approved drugs against SARS-CoV-2 in human lung cells: Nafamostat is the most potent antiviral drug candidate.* bioRxiv, 2020: p. 2020.05.12.090035.
46. Thapar, M.M., et al., *Time-dependent pharmacokinetics and drug metabolism of atovaquone plus proguanil (Malarone) when taken as chemoprophylaxis.* European Journal of Clinical Pharmacology, 2002. **58**(1): p. 19-27.
47. Zsila, F. and I. Fitos, *Combination of chiroptical, absorption and fluorescence spectroscopic methods reveals multiple, hydrophobicity-driven human serum albumin binding of the antimalarial atovaquone and related hydroxynaphthoquinone compounds.* Org Biomol Chem, 2010. **8**(21): p. 4905-14.
48. Hussein, Z., et al., *Population pharmacokinetics of atovaquone in patients with acute malaria caused by Plasmodium falciparum.* Clin Pharmacol Ther, 1997. **61**(5): p. 518-30.
49. Cifuentes Kottkamp, A., et al., *Atovaquone Inhibits Arbovirus Replication through the Depletion of Intracellular Nucleotides.* J Virol, 2019. **93**(11).
50. Naccarelli, G.V., et al., *Safety and efficacy of dronedarone in the treatment of atrial fibrillation/flutter.* Clinical Medicine Insights. Cardiology, 2011. **5**: p. 103-119.
51. Braithwaite, P.A., et al., *Clinical pharmacokinetics of high dose mebendazole in patients treated for cystic hydatid disease.* Eur J Clin Pharmacol, 1982. **22**(2): p. 161-9.
52. SELDEN, R., T.W. SMITH, and W. Findley, *Ouabain Pharmacokinetics in Dog and Man.* Circulation, 1972. **45**(6): p. 1176-1182.
53. Naim, M., et al., *Solvated interaction energy (SIE) for scoring protein-ligand binding affinities. 1. Exploring the parameter space.* J Chem Inf Model, 2007. **47**(1): p. 122-33.
54. Neudert, G. and G. Klebe, *DSX: a knowledge-based scoring function for the assessment of protein-ligand complexes.* J Chem Inf Model, 2011. **51**(10): p. 2731-45.
55. Shirato, K., M. Kawase, and S. Matsuyama, *Middle East respiratory syndrome coronavirus infection mediated by the transmembrane serine protease TMPRSS2.* J Virol, 2013. **87**(23): p. 12552-61.